crystals

MDPI

Article

Titanite Spectroscopy and In Situ LA-ICP-MS U–Pb Geochronology of Mogok, Myanmar

Jialu Gu [1], Bo Xu [2,*], Shu Li [2] and Yi Zhao [1]

[1] School of Earth Sciences and Resources, China University of Geosciences Beijing, 29 Xueyuan Road, Haidian District, Beijing 100083, China; 3001210024@email.cugb.edu.cn (J.G.); zhaoyi0102@cugb.edu.cn (Y.Z.)

[2] School of Gemmology, China University of Geosciences Beijing, 29 Xueyuan Road, Haidian District, Beijing 100083, China; 2009200038@cugb.edu.cn

* Correspondence: bo.xu@cugb.edu.cn

Abstract: With the development of mineral testing technology and ore deposit geochemistry, titanite has become a hot topic in the study of accessory minerals. Two large-grained titanite crystals from Mogok, Myanmar, were used for a detailed study. In this study, the standard gemmological properties and spectral characteristics of titanite crystals were obtained by Fourier transform in-frared, micro ultraviolet-visible-near-infrared and Raman spectroscopy, respectively, which pro-vide a full set of data. Mineral major and trace elements were analysed using Electron-Probe Mi-croAnalysis (EPMA) and Laser Ablation Inductively Coupled Plasma Mass Spectrometry (LA-ICP-MS). The purpose of this study is to report spectral characteristics and major and trace elements of Mogok, Myanmar, in order to find new potential titanite standard samples. The two titanite crystals have similar major element compositions, and both grains have relatively low Al content (0.011–0.014 apfu) and Al/Fe ratios (0.157–0.222), but high Fe content (0.063–0.079 apfu). The two titanite crystals have similar chondrite-normalised rare earth element (REE) patterns with significantly Light Rare Earth Element (LREE) (La–Gd) enrichment and deletion of Heavy Rare Earth Element (HREE) (Tb–Lu). The $^{238}U/^{206}Pb$ ages of the two titanite samples are 43.5 ± 5.8 Ma and 34.0 ± 4.2 Ma, respectively. Generally, magmatic titanite has a low Al/Fe ratio, metamorphic and hydrothermal titanite crystals have extremely low Th/U ratios close to zero, with flat chondrite-normalised REE patterns or depletions in light REEs relative to heavy REEs. Different genetic types of titanite can be distinguished by the characteristics of major and trace elements. Combined chemical features such as REE differentiation, Al/Fe and Th/U ratios with formation temperature, the analysed titanite samples are considered magmatic-hydrothermal titanites. Their $^{238}U/^{206}Pb$ ages may indicate a potential stage of magmatic hydrothermal conversion.

Keywords: titanite; U–Pb dating; LA-ICP-MS; major and trace elements

check for updates

Citation: Gu, J.; Xu, B.; Li, S.; Zhao, Y. Titanite Spectroscopy and In Situ LA-ICP-MS U–Pb Geochronology of Mogok, Myanmar. *Crystals* **2022**, *12*, 1050. https://doi.org/10.3390/cryst12081050

Academic Editor: Per-Lennart Larsson

Received: 7 June 2022
Accepted: 18 July 2022
Published: 28 July 2022

1. Introduction

Titanite ($CaTiSiO_5$) is a common accessory mineral in various geological environments, including calc-alkalic plutonic rocks [1] (particularly I-type granites), metamorphic rocks [2] and hydrothermal products such as skarns [3]. The crystal structure of titanite is connected by SiO_4 tetrahedron and TiO_6 octahedron, and Ca^{2+} cations exist in the lattice with 7 coordination number [4]. The Ca^{2+} site can accommodate all large cations, including Y, rare earth elements (REEs), U, Th, Mn and Pb. These elements can indicate magmatic or hydrothermal evolution, which makes titanite a useful indicator of magma and/or fluid characteristics [5–9]. In addition, titanite is a good U–Th–Pb radiometric chronometer [10–15].

Recently, laser ablation multi-collector inductively coupled plasma mass spectrometry (LA-MC-ICP-MS) instrumentation has been widely used to determine the in situ major trace element and isotopic compositions of titanites [1,14,16–28]. However, the lack of matrix matching standard materials is a significant barrier to the widespread adoption of this technology [29].

In this study, in situ major trace element compositions of two titanite single crystals in Mogok, Myanmar, have been studied through electron probe microanalysis (EPMA) and LA-MC-ICP-MS. Spectral features are obtained and compared with the calibration spectra in the RRUFF database [30]. Our aims were to establish potential young titanite standard samples and reveal the genesis of titanite.

2. Geological Setting

The Mogok area in Myanmar is a world-famous gem-producing area (Figure 1a) [31–33], which, extending in the north–south direction, is primarily composed of metamorphic rocks, mixed rocks and late Mesozoic granitic intrusive rocks (Figure 1b) [34–36]. The Mogok metamorphic zone was formed by the northward subduction of the Indian plate in 71 Ma and the collision between the Eurasian and Indian plate at approximately 50 Ma [37]. Previous studies show that deep crustal melting occurred with ages ranging from 20–15 Ma in this region, and this process was accompanied by granite intrusion. Precious age determinations indicate that metamorphism along the MMB occurred during 68–21 Ma with peak between the Middle Eocene and the early Oligocene [38–41]. The Mogok titanite samples can meet the requirement of younger standard samples.

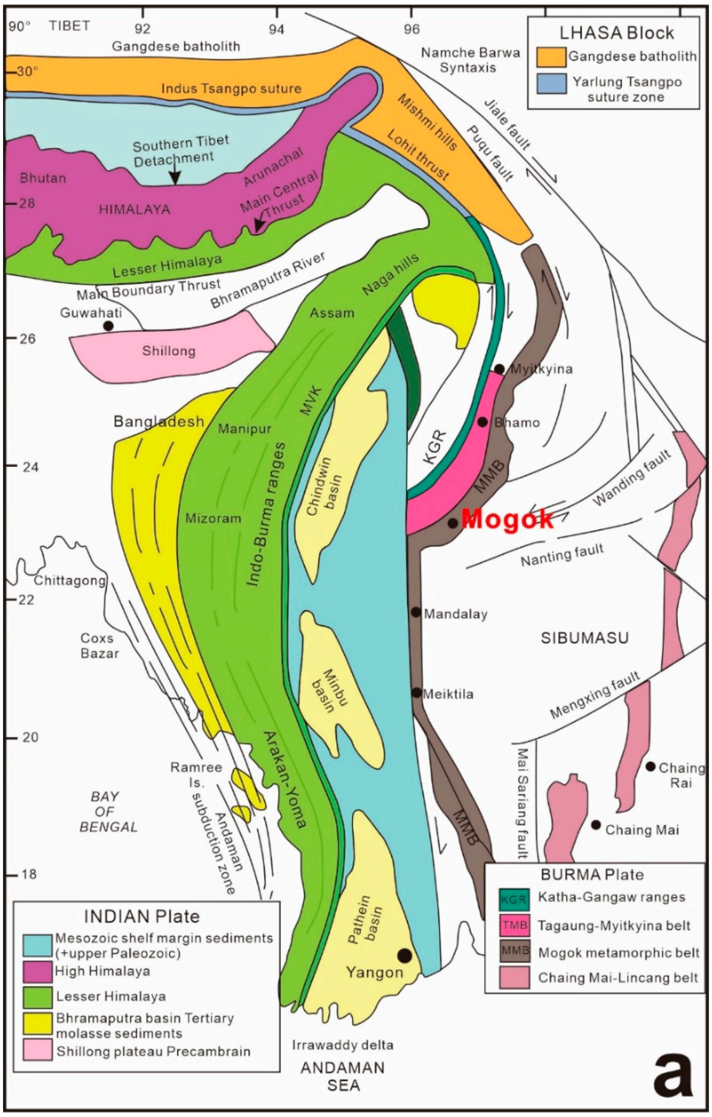

Figure 1. *Cont.*

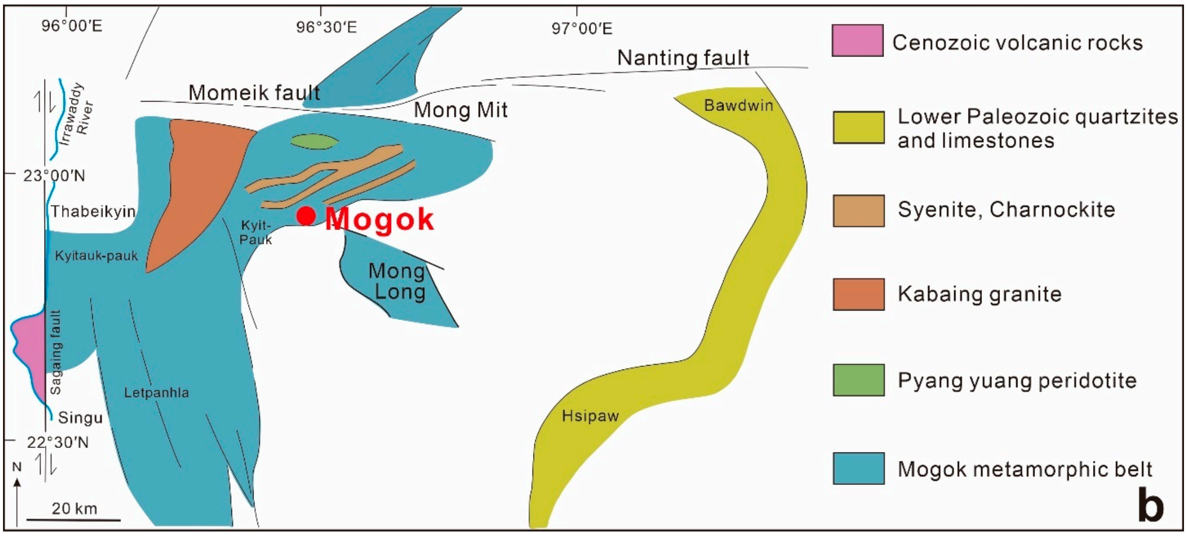

Figure 1. Geological maps of Mogok metamorphic belt and adjacent regions (modified from Win et al., 2018) (**a**) [42]. The main geological structures for the Mogok area (modified from Searle et al., 2020) (**b**) [39].

3. Materials and Methods

Two Mogok titanite crystals (MG-5 and MG-6) were examined using standard gemmological techniques. The specific gravity (SG) of the samples was obtained using a hydrostatic weighing method. Spectroscopy tests for the samples were conducted at the Gemmological Research Laboratory of China University of Geosciences (Beijing) to obtain their spectral properties.

Infrared reflection spectra were obtained using the Tensor 27 Fourier transform infrared spectrometer, with a test spectral range of 2000–400 cm^{-1}. An ultraviolet–visible (UV–Vis) spectroscopy test was conducted using a UV-3600 UV–Vis spectrophotometer (Shimadzu Corporation, Kyoto, Japan) to measure the absorption value with the following setting: slit width: 2.0 nm; time constant: 0.1 s; wavelength range (nm): 200.00–900.00; scanning speed: high speed; sampling interval: 0.5 A Horiba HR Evolution-type microconfocal laser Raman spectrometer (Horiba, Ltd., Kyoto, Japan), which was used to conduct a Raman spectroscopy test with the following setting: laser source: 532 nm; slit width: 100 μm; grating: 600 gr/mm; scan time: 4 s; integration times: 3; ICS correction range: 100–2000 cm^{-1}.

The titanite grains were mounted in epoxy, polished and examined using BSE images to select suitable targets for in situ analysis. The TESCAN field emission scanning electron microscope (MIRA 3LMH) was used to capture BSE images with the following setting: acceleration voltage: 7 kV; absorption current: 1.2 Na; scan time: 80 s.

Electron-Probe MicroAnalysis (EPMA) was conducted in the Laboratory of EPMA, China University of Geosciences (Beijing) with the following setting: acceleration voltage: 15 kV; electic current: 10 Na; beam spot diameter: 1 μm.

An Agilent 7900 Q-ICP-MS instrument coupled to a 193-nm ArF excimer laser ablation system was used to determine trace element compositions and U–Pb ages in the Laboratory of Mineral Laser Microzone Analysis, China University of Geosciences (Beijing). The Ontario standard was used for calibration, and the MKED1 standard was used as a standard reference.

4. Results

4.1. Visual Appearance and Gemmological Properties

The titanite samples are dark brown and translucent with medium cleavage and greasy lustre (Figure 2a,b). The MG-6 sample has crystal plane steps. Triangular etching on the crystal surface can also be observed. Some weak areas of MG-5 sample are dissolved into small pits by corrosion, forming regular shaped pits on the crystal surface (Figure 3).

Figure 2. The titanite crystals of MG-5 (**a**) and MG-6 (**b**).

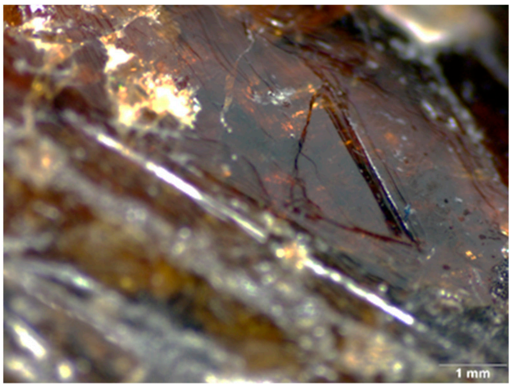

Figure 3. Triangular etching of MG-5.

The SG values of MG-5 and MG-6 are 3.51 and 3.56, respectively. Since the refractive index of titanite varied between 1.89 and 2.02, the index of refraction exceeded the refractometer's value and could not be measured. The titanite samples do not change colour under a Chelsea colour filter. The titanite samples have a rare earth spectrum, as seen through spectroscopes, with multiple fine absorption lines and 580 nm double lines.

4.2. Spectral Characteristics

4.2.1. Fourier Transform Infrared Spectrum

The MG-5 and MG-6 samples have 432.04, 565.12, 725.21 and 939.30 cm^{-1} characteristic absorption peaks in the fingerprint region (Figure 4). The position of 420–440 cm^{-1} is the vibration band of TiO_6 octahedron. The position of 550–570 cm^{-1} is the in-plane bending vibration band of $SiO_4{}^{4-}$ and Si–O bond; the position of 730 cm^{-1} is the stretching vibration band of Si–Si bond; and 800–1000 cm^{-1} is the position of the asymmetric stretching vibration band of the Si–O bond and triple simplification of $SiO_4{}^{4-}$.

4.2.2. UV–Vis Spectrum

The colour origin of the titanite samples was analysed by UV–Vis spectra. MG-5 and MG-6 are brown titanite samples. The UV–Vis spectrum of MG-6 has an obvious absorption peak centred at 565 nm in the range of 550–600 nm, weak absorption peaks at 700–800 nm and a wide and slow absorption band at 220–300 nm (Figure 5). The yellow–green absorption band with 565 nm as the centre in the range of 550–600 nm is caused by the electron transition between Ti^{4+} and Fe^{4+}.

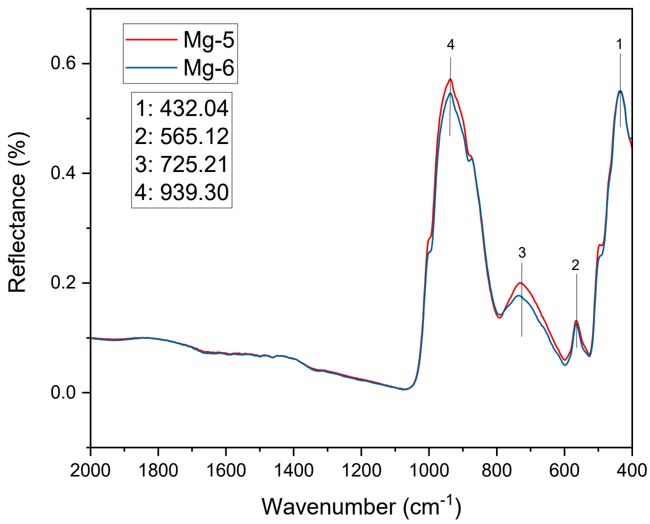

Figure 4. Fourier Transform Infrared Spectrum of MG-5 and MG-6.

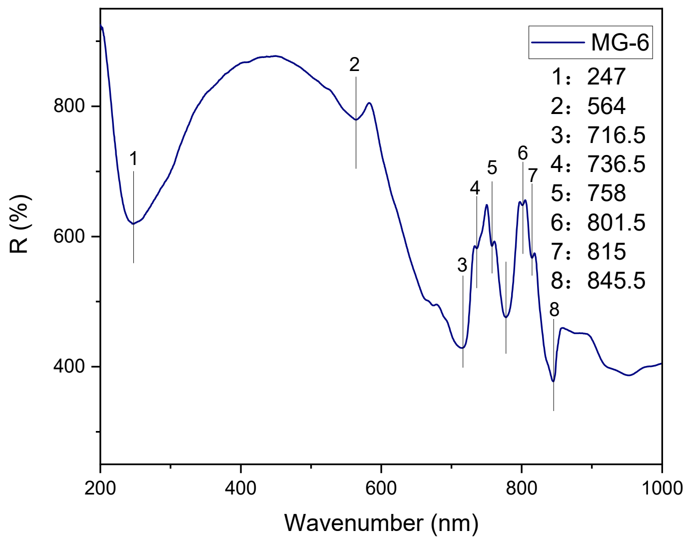

Figure 5. UV–Vis spectrum of MG-6.

4.2.3. Raman Spectrum

The following characteristic peaks of the titanite samples are found within the range of 200–2000 cm^{-1}: an absorption peak at 242 cm^{-1} caused by the translational vibration of $[SiO_4]^{4+}$, an absorption peak at 316 cm^{-1} caused by the rotational vibration of $[SiO_4]^{4+}$, an absorption peak at 467 cm^{-1} caused by the bending vibration of $[SiO_4]^{4+}$, a strong absorption peak at 605 cm^{-1} and an absorption peak at 854 cm^{-1} both caused by the stretching vibration of $[SiO_4]^{4+}$ (Figure 6).

4.3. Major and Trace Elements

Major element compositions of the titanite samples are presented in Table 1. The two titanite crystals have similar major element compositions (CaO 25.93–27.61 wt%, TiO_2 36.67–38.25 wt% and SiO_2 29.50–30.47 wt%). Both grains show relatively low Al contents (0.15–0.18 apfu) and low Al/Fe ratios (0.07–0.08), but high Fe content (1.77–2.22 apfu).

Forty analyses were conducted on the two titanite grains by LA-MC-ICP-MS. The trace element compositions are listed in Tables 2 and 3 Titanite is an essential sink of the entire rock [43], Nb, Ta, Th and U (Nb: 203.6–846.8 ppm; Ta: 2.181–19.23 ppm; Th: 0.892–3.412 ppm; U: 0.6871–3 ppm), and is commonly enriched with LREEs. The two titanite crystals have similar chondrite-normalised REE patterns with moderate REE concentrations (REE: 1896–2857 ppm). They have significantly LREE enrichment and deletion of HREE (LREE/HREE: 6.55–10.39) (Figure 7a,b).

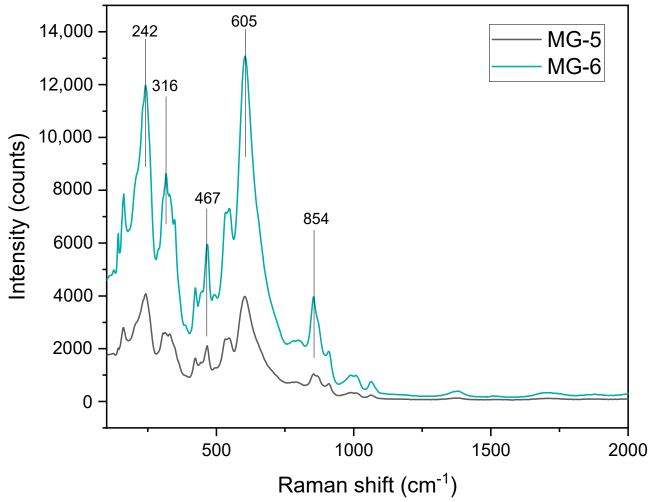

Figure 6. Raman spectra of MG-5 and MG-6.

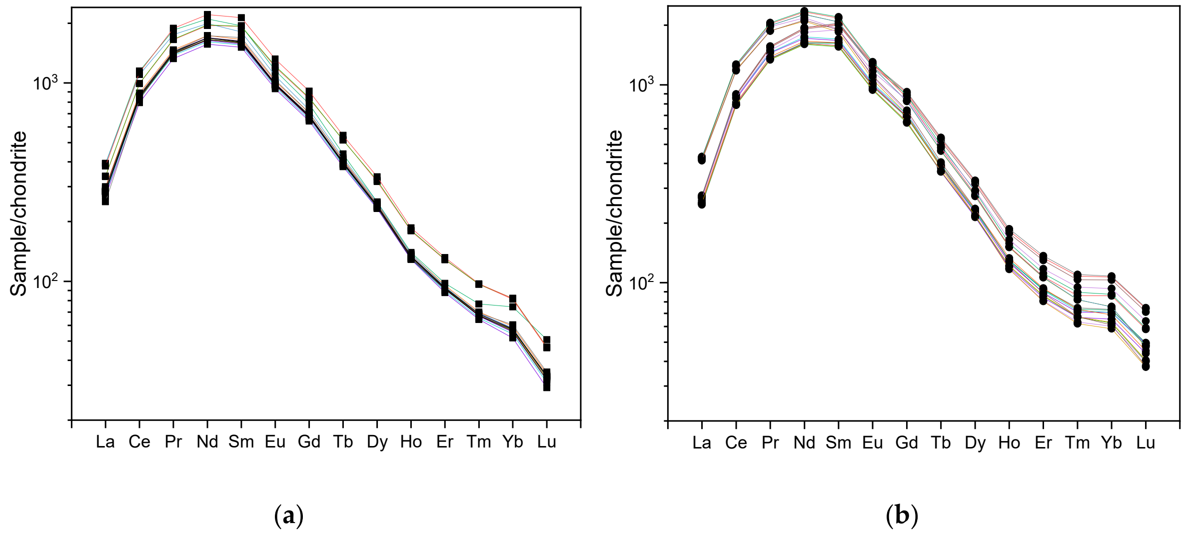

Figure 7. Chondrite-normalised REE patterns of titanite samples MG-5 (**a**) and MG-6 (**b**). Chondrite REE values from McDonough, W.F. and Sun, S.S. (1995) [44]. Lines with different colors represent data of different spots in measurement by LA-ICP-MS.

Previous studies have demonstrated that REEs replace Ca and Zr in titanite and high field strength elements such as Nd will displace Ti (Al, Fe) in the titanite lattice. The positive correlation of Nd–Zr in the samples shows that the two elements exhibit the same substitution characteristics (Figure 8).

4.4. Titanite U–Pb Ages

The titanite ages with common Pb [45] were calculated using the weighted mean of the ^{207}Pb-corrected ages and the Tera–Wasserberg (TW) Concordia intercept age anchored through common Pb. Titanite U–Pb isotope results and ages are listed in Tables 4 and 5. Overall 20 LA-ICP-MS analyses of each titanite sample were performed in different sections (Figure 9a,b). On the TW diagram, the common Pb-uncorrected data of MG-5 define a linear array, yielding a lower-intercept age of 44 ± 17 Ma (n = 20, 2σ, MSWD = 0.63) and a y-intercept of initial $^{207}Pb/^{206}Pb$ of 0.848 (Figure 10a,b). The common Pb-uncorrected data of MG-6 define a linear array, yielding a lower-intercept age of 34 ± 14 Ma (n = 20, 2σ, MSWD = 0.75) and a y-intercept of initial $^{207}Pb/^{206}Pb$ of 0.843 (Figure 10c,d). On the basis of this common Pb composition, a common Pb correction was performed using the method of fitting $^{207}Pb/^{206}Pb_c$. All analyses of MG-5 yielded a weighted average $^{206}Pb/^{238}U$ age of 43.5 ± 5.8 Ma (n = 20, 2σ, MSWD = 0.57), and those of MG-6 yielded a weighted average $^{206}Pb/^{238}U$ age of 34.0 ± 4.2 Ma (n = 20, 2σ, MSWD = 0.65).

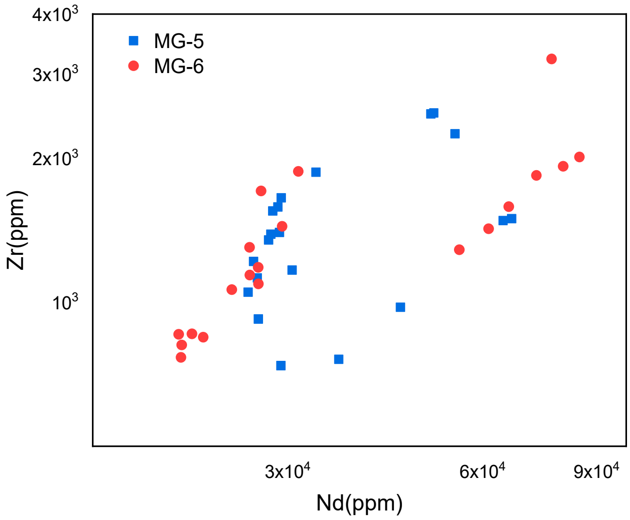

Figure 8. Correlations between Nd (ppm) and Zr (ppm) of titanites.

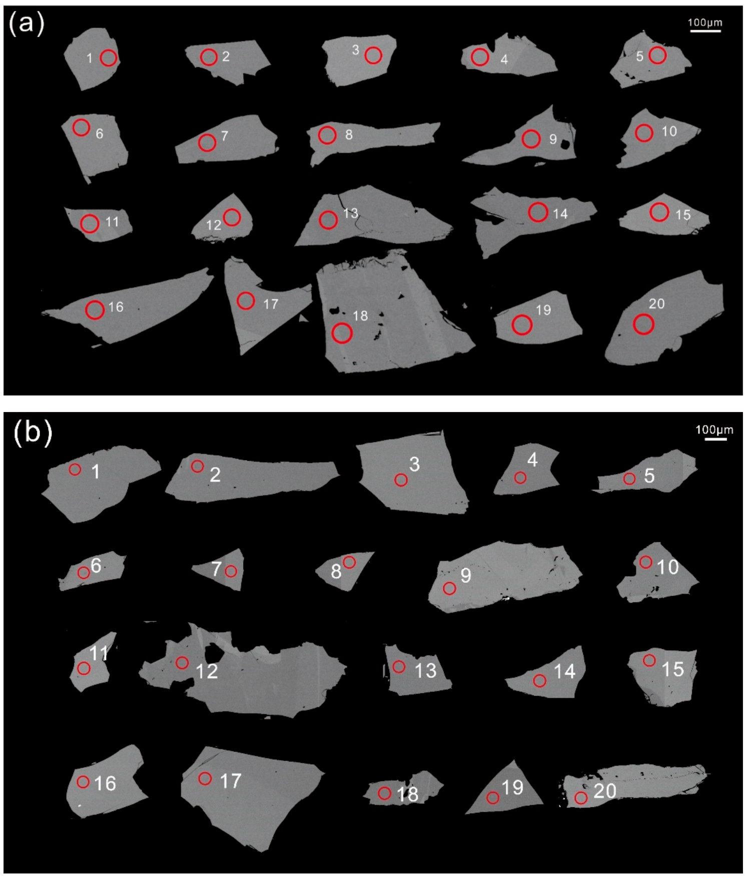

Figure 9. Backscattered electron images of the Mogok titanites MG-5 (**a**) and MG-6 (**b**). Red circles show positions for simultaneous LA-ICP-MS measurements of U–Pb ages. $^{206}Pb/^{238}U$ ages are in red.

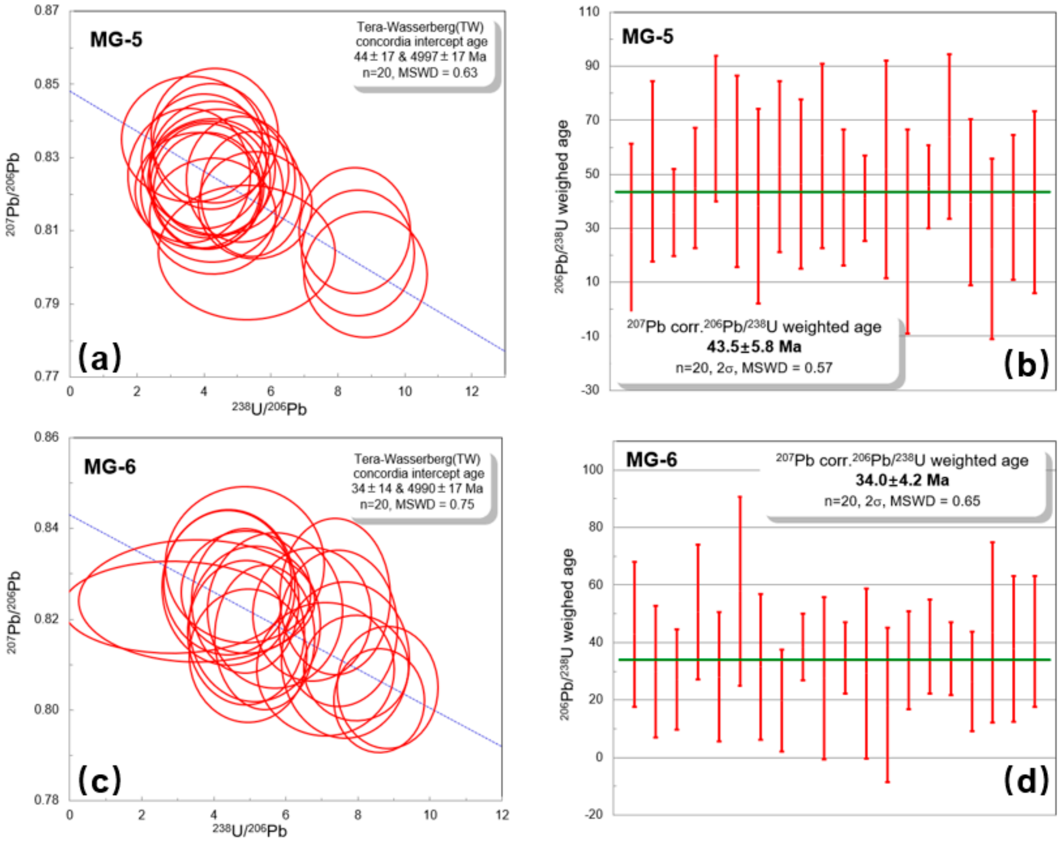

Figure 10. LA-ICP-MS titanite U–Pb TW diagram (**a**) and $^{206}Pb/^{238}U$ weighed age for MG-5 (**b**); LA-ICP-MS titanite U–Pb TW diagram (**c**) and $^{206}Pb/^{238}U$ weighed age for MG-6 (**d**).

5. Discussion

5.1. Comparision with RRUFF Database

The RRUFF database contains eight titanite standard samples from Brazil, the USA, Pakistan, Canada and Mexico. R050114 with yellowish-brown fragments from Pakistan was chosen for comparison. Fourier transform infrared spectra of titanite R050114 have 416.5, 559.3 and 848.5 cm^{-1} characteristic absorption peaks in the fingerprint region (Figure 11), indicating that these characteristic peaks occur in the range of peaks caused by different bonds; however, the positions of these characteristic peaks are different. Raman spectra of titanite R050114 have 252, 316, 423, 605, 873, 880 and 1177cm^{-1} characteristic peaks (Figure 12). The characteristic peak at 605 cm^{-1} is consistent with that of the analysed samples MG-5 and MG-6.

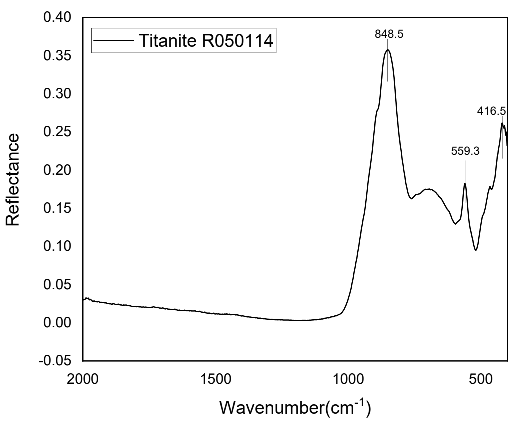

Figure 11. Fourier transform infrared spectrum of titanite R050114 from RRUFF database.

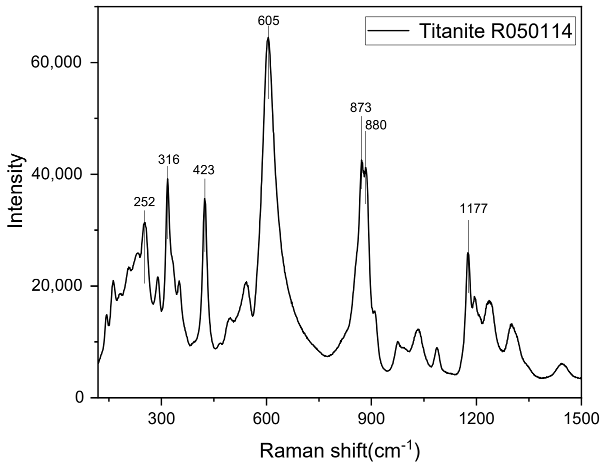

Figure 12. Raman spectrum of titanite R050114 from RRUFF database.

Raman spectra of common titanite reference samples are shown in Figure 13 [46]. All samples exhibited characteristic peaks near 255, 316, 342 and 850 cm^{-1}, similar to analysed samples MG-5 and MG-6. The Raman spectra of the YQ82, BMB108 and MKED1 samples are similar, with characteristic peaks at 162, 231, 250, 540, 606 and 911 cm^{-1}. The Raman spectra of the BLR-1, Ontario and OLT1 titanite samples are similar, with characteristic peaks at 573 and 650 cm^{-1}. Bands occurred near 575 and 611 cm^{-1} in the Khan titanite, rendering this an intermediate sample between the above two groups.

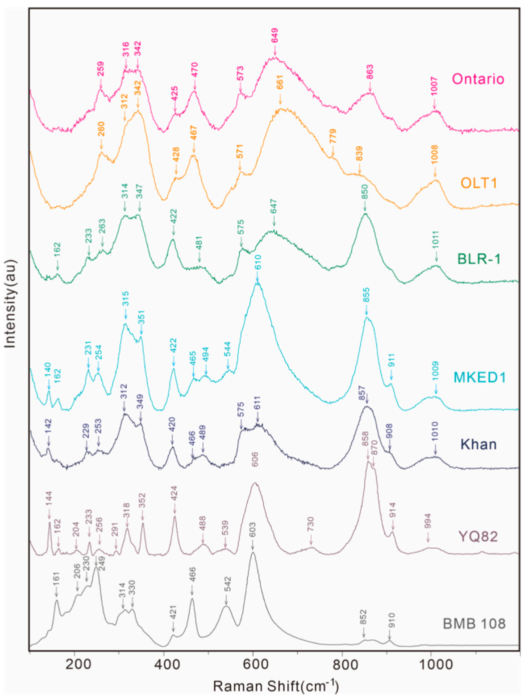

Figure 13. Raman spectra of common titanite reference samples (modified from a part of Figure 3 of Ling X-X et al., 2022) [46].

5.2. Formation Temperature of Titanite

The Al_2O_3 content of titanite was used to estimate the formation pressure of titanite [47], and a pressure-dependent Zr in titanite geothermometer [48] was used to estimate the formation temperature of titanite. High temperatures enable more Zr to enter the structure of titanite. The Al_2O_3 content of titanite increases with pressure (P) according to the following: P (in MPa) = 101.66 × Al_2O_3 in titanite (in wt%) + 59.013 (R^2 = 0.83). The pressures of MG-5 were estimated to be 88.39–92.15 Mpa (average = 90.14 Mpa, n = 10), and those of MG-6 were estimated to be 86.56–94.80 Mpa (average = 92.04 Mpa, n = 10). According to the studies by Hayden et al. (2008), $\alpha_{TiO2} = \alpha_{SiO2} = 1$. The Zr in titanite temperatures of MG-5 were estimated to be 466.5–467.1 °C (average = 466.79 °C, n = 20), and those of MG-6 were estimated to be 466.6–467.2 °C (average = 466.98 °C, n = 20).

Along with the weighted average $^{206}Pb/^{238}U$ ages of these two samples, the calculated temperature range is consistent with the geological background of their ages (Figure 14). However, there is a significant difference in the calculation results of temperature, which may be caused by the inaccuracy of cogenetic minerals in the calculation formula.

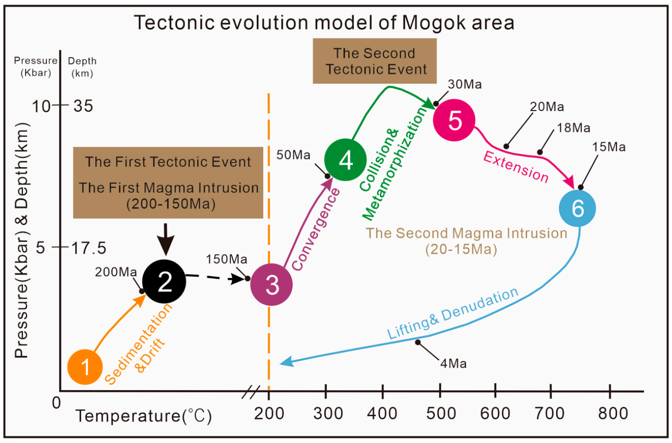

Figure 14. Tectonic evolution model of Mogok area (modified from Themelis et al., 2008) [37].

5.3. Genesis of Analysed Titanite

The classification of the genetic types of titanite requires comprehensive consideration of the major and trace elements. In general, magmatic titanite has a low Al/Fe ratio, whereas metamorphic titanite, including hydrothermal titanite, has a high Al/Fe ratio. Both grains have been plotted in the igneous field of Kowallis et al. (1997) (Figure 15).

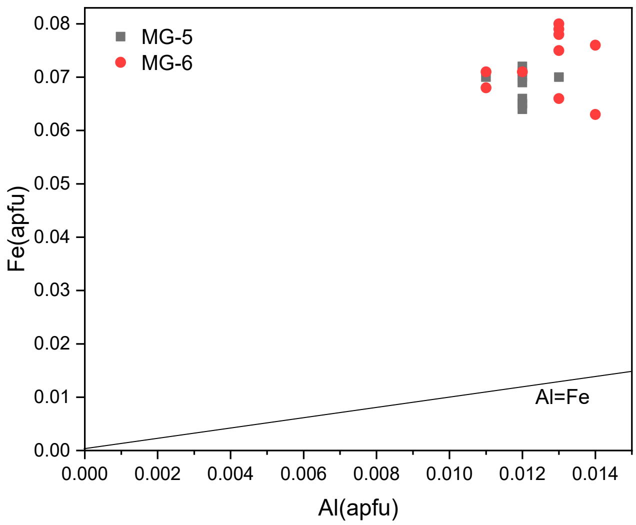

Figure 15. Fe vs. Al cations per formula unit.

Metamorphic and hydrothermal titanite crystals commonly have extremely low Th/U ratios close to zero, along with flat chondrite-normalised REE patterns or depletions in light REEs relative to heavy REEs. In contrast, two analysed titanite grains show heavy light REE (La–Gd) to weak heavy REEs (Tb–Lu) differentiation [49].

The Th/U ratio is also an indicator of the origin of titanite. In general, hydrothermal titanite has a lower ratio of Th/U (mostly < 1) than magmatic titanite. In this study, the two samples yielded a similar ratio of Th/U (MG-5: 1.30–1.92; average: 1.61; MG-6: 1.08–1.57; average: 1.37). Thus, titanite that crystallises under high-temperature hydrothermal conditions would also have the characteristics of magmatic titanite Th/U > 1. To discriminate the origin of titanite using a single ratio of Th/U indicator is inaccurate.

However, considering that the calculated formation temperatures were lower and consistent with that of the hydrothermally modified titanite, EMPA data have shown low concentrations of La in the analysed titanite samples (Table 5), which is commonly related to late hydrothermal activity [50], and our samples can be recognized as products of magmatic hydrothermal conversion [27,51,52].

Analysed titanite samples are interpreted as magmatic-hydrothermal.

5.4. Tectonic Evolutionary History

Themelis (2007) divides the geological evolution of Mogok into six important stages: deposit, continental drift, plate convergence, continental plate collision, post-collisional extension, lifting and erosion (Figure 14). The continental plate collision occurred between 50 Ma and 30 Ma, and the Northeastern Indian plate subducted obliquely into the Eastern Asian plate. Continental collisions and the drift and collision of other microland masses continue today. The weighted average $^{206}Pb/^{238}U$ ages of the two titanite crystals are determined as 43.5 ± 5.8 Ma and 34.0 ± 4.2 Ma, respectively, limiting the formation age of titanite in the period of continental plate collision.

6. Conclusions

We have investigated the chemical composition, structure and genesis of titanite crystals from Mogok, Myanmar, through Fourier infrared, UV–Vis and Raman spectroscopy, EPMA and LA-MC-ICP-MS. These results are used to assess the potential of titanite as reference material for micro-analytical dating. In this paper, the analysis and summary of mineralogical and spectral characteristics based on the samples provide characteristics of a new production area of titanite not found in the RURFF database. According to U–Pb dating analysis, age data have a high concordant degree with weighted average $^{206}Pb/^{238}U$ ages 43.5 ± 5.8 Ma and 34.0 ± 4.2 Ma, respectively, which indicates the potential stage of magmatic hydrothermal conversion. Thus, these two grains can be used as potential stand samples for U–Pb dating analysis. Major and trace element analyses of titanites can be used to discuss the genetic type and explore their geological background.

Author Contributions: Writing and experimental data processing, J.G.; writing—review and editing, B.X., S.L. and Y.Z.; methodology, B.X.; software, J.G. and S.L. All authors have read and agreed to the published version of the manuscript.

Funding: This research was funded by National Key Technologies R&D Program (2020YFA0714800, 2019YFA0708602); National Natural Science Foundation of China (42073038, 41803045), Young Talent Support Project of CAST, the Fundamental Research Funds for the Central Universities (Grant no. 265QZ2021012), and IGCP-662.

Data Availability Statement: The data presented in this study are available within this article.

Acknowledgments: We thank the editor and reviewers for constructive comments which helped in improving our paper. This is the 8th contribution of B.X. for the National Mineral Rock and Fossil Specimens Resource Center.

Conflicts of Interest: The authors declare no conflict of interest.

Appendix A

Table 1. Chemical compositions with the structural formulas of analysed titanite from Mogok analysed by EMPA (wt.%).

			MG-5-1	MG-5-2	MG-5-3		MG-5-4	MG-5-5	MG-5-6	MG-5-7	MG-5-8		MG-5-9	MG-5-10	MG-6-1	MG-6-2	MG-6-3	MG-6-4	MG-6-5	MG-6-6	MG-6-7	MG-6-8	MG-6-9	MG-6-10
SiO_2			29.904	30.071	29.686		29.504	30.033	30.125	29.555	29.954		29.962	30.069	30.219	30.094	30.177	29.889	29.779	30.47	29.619	29.733	29.979	30.032
TiO_2			37.147	36.929	38.246		38.016	37.133	38.153	37.695	38.016		37.371	37.324	37.037	36.668	37.176	37.662	37.977	37.417	37.951	37.224	37.099	37.497
Al_2O_3			0.308	0.303	0.326		0.312	0.301	0.308	0.31	0.304		0.289	0.301	0.277	0.343	0.331	0.348	0.342	0.352	0.271	0.338	0.334	0.313
FeO			2.488	2.322	2.533		2.587	2.299	2.567	2.456	2.353		2.485	2.308	2.554	2.811	2.825	2.722	2.364	2.283	2.405	2.855	2.669	2.547
MnO			0.044	0.014	0.039		0	0	0	0	0		0.004	0.092	0.012	0	0.016	0.014	0.025	0.045	0.143	0	0	0.131
MgO			0.029	0.008	0.042		0.009	0	0.01	0.012	0.008		0.019	0.029	0.036	0.017	0.025	0.021	0.009	0.024	0.013	0.037	0.028	0.005
CaO	26.839	27.075	26.363	26.559	26.748	26.477	27.119	26.459	26.519	26.578	26.994	27.612	26.707	27.065	26.553	26.376	26.583	26.259		25.928			26.975	
Na_2O	0.431	0.44	0.552	0.518	0.441	0.43	0.388	0.422	0.425	0.44	0.381	0.343	0.413	0.369	0.599	0.511	0.393	0.456		0.591			0.345	
K_2O	0.013	0	0.007	0.009	0.008	0	0.014	0.005	0.002	0.018	0.001	0.007	0.012	0.02	0	0.014	0.006	0.008		0.02			0.002	
F	0.179	0.131	0.151	0.13	0.377	0.097	0.193	0.172	0.22	0.213	0.248	0.315	0.001	0.001	0.14	0.21	0.013	0.396		0.049			0.055	
Cr_2O_3	0.008	0	0	0	0.036	0	0	0	0.016	0.081	0	0.028	0.007	0	0	0.055	0	0.025		0			0	
NiO	0.035	0.009	0	0.067	0.078	0.057	0.051	0.002	0	0	0.016	0	0	0	0.019	0.066	0	0.028		0.079			0.073	
V_2O_5	0.385	0.485	0.522	0.422	0.358	0.333	0.383	0.477	0.4	0.363	0.521	0.447	0.488	0.377	0.371	0.52	0.332	0.522		0.415			0.458	
La_2O_3	0	0.033	0	0.064	0	0	0	0	0.104	0	0	0.007	0	0	0	0.141	0.007	0.097		0			0	
Ce_2O_3	0.816	0.9	1.193	1.414	0.918	0.705	0.918	0.997	0.891	1.092	0.768	0.948	0.833	0.985	1.195	1.097	0.958	0.736		1.089			1.062	
Total	98.627	98.719	99.66	99.612	98.73	99.26	99.095	99.169	98.709	98.906	99.066	99.642	99.01	99.472	99.373	99.58	98.696	98.714		98.28			99.495	
Cations (apfu)																								
Si	1.003	1.008	0.988	0.986	1.003	1.002	0.988	0.998	1.003	1.005	1.007	1.001	1.010	0.998	0.993	1.011	0.995	0.995		1.011			1.002	
Al	0.012	0.012	0.013	0.012	0.012	0.012	0.012	0.012	0.011	0.012	0.011	0.013	0.013	0.014	0.013	0.014	0.011	0.013		0.013			0.012	
Ti	0.937	0.931	0.957	0.955	0.933	0.955	0.948	0.953	0.941	0.938	0.929	0.917	0.936	0.946	0.953	0.934	0.959	0.937		0.941			0.941	
Fe	0.070	0.065	0.070	0.072	0.064	0.071	0.069	0.066	0.070	0.065	0.071	0.078	0.079	0.076	0.066	0.063	0.068	0.080		0.075			0.071	
Mn	0.001	0.000	0.001	0.000	0.000	0.000	0.000	0.000	0.000	0.003	0.000	0.000	0.000	0.000	0.001	0.001	0.004	0.000		0.000			0.004	
Mg	0.001	0.000	0.002	0.000	0.000	0.000	0.001	0.000	0.001	0.001	0.002	0.001	0.001	0.001	0.000	0.001	0.001	0.002		0.001			0.000	
Ca	0.964	0.972	0.940	0.951	0.957	0.944	0.972	0.945	0.951	0.952	0.964	0.984	0.958	0.968	0.949	0.938	0.957	0.941		0.936			0.964	
Na	0.028	0.029	0.036	0.034	0.029	0.028	0.025	0.027	0.028	0.029	0.025	0.022	0.027	0.024	0.039	0.033	0.026	0.030		0.039			0.022	
K	0.001	0.000	0.000	0.000	0.000	0.000	0.001	0.000	0.000	0.001	0.000	0.000	0.001	0.001	0.000	0.001	0.000	0.000		0.001			0.000	
F	0.019	0.014	0.016	0.014	0.040	0.010	0.020	0.018	0.023	0.023	0.026	0.033	0.000	0.000	0.015	0.022	0.001	0.042		0.005			0.006	
Cr	0.000	0.000	0.000	0.000	0.001	0.000	0.000	0.000	0.000	0.002	0.000	0.001	0.000	0.000	0.000	0.001	0.000	0.001		0.000			0.000	
Ni	0.001	0.000	0.000	0.002	0.002	0.002	0.001	0.000	0.000	0.000	0.000	0.000	0.000	0.000	0.001	0.002	0.000	0.001		0.002			0.002	
V	0.010	0.013	0.014	0.011	0.010	0.009	0.010	0.013	0.011	0.010	0.014	0.012	0.013	0.010	0.010	0.014	0.009	0.014		0.011			0.012	
La	0.000	0.000	0.000	0.001	0.000	0.000	0.000	0.000	0.001	0.000	0.000	0.000	0.000	0.000	0.000	0.002	0.000	0.001		0.000			0.000	
Ce	0.010	0.011	0.015	0.017	0.011	0.009	0.011	0.012	0.011	0.013	0.009	0.012	0.010	0.012	0.015	0.013	0.012	0.009		0.013			0.013	

Table 2. Rare earth element content (ppm) of MG-5.

	La	Ce	Pr	Nd	Sm	Eu	Gd	Tb	Dy	Ho	Er	Tm	Yb	Lu
MG-5-1	66.78	517.4	129.8	748.5	232.6	54.66	132.7	14.26	58.06	7.215	14.68	1.648	8.94	0.784
MG-5-2	67.10	522.8	131.1	758.9	237.6	55.37	135.7	14.46	59.12	7.359	14.94	1.699	9.23	0.8233
MG-5-3	79.89	607.7	153.2	889.1	284.8	67.84	166.3	18.67	78.31	9.806	20.55	2.386	13.09	1.138
MG-5-4	92.81	703.2	171.2	961	287	65.01	155.9	15.83	61.89	7.636	15.64	1.899	11.99	1.252
MG-5-5	68.72	531.4	133.7	773.9	240.7	56.22	135.8	14.50	59.56	7.355	14.83	1.693	9.33	0.8161
MG-5-6	66.88	515.4	129.9	753.2	235.6	54.84	134.1	14.24	58.14	7.236	14.74	1.668	9.10	0.811
MG-5-7	65.41	508.4	127.9	737.4	229.5	53.79	130.3	13.91	57.4	7.081	14.29	1.615	8.74	0.760
MG-5-8	67.35	519.0	130.2	758.4	235.4	55.19	135.2	14.35	58.74	7.289	14.82	1.67	9.13	0.803
MG-5-9	67.61	519.7	130.3	757.1	236.3	55.28	134.6	14.36	59.14	7.294	14.79	1.663	9.11	0.794
MG-5-10	70.98	544.2	136.0	791.1	245.1	57.46	140.3	14.82	60.63	7.495	15.27	1.732	9.55	0.840
MG-5-11	93.26	674.7	162.5	909.4	267.1	61.19	145.5	15.14	61.63	7.506	15.04	1.707	9.35	0.811
MG-5-12	80.34	609.1	153.9	896.5	285.6	68.46	167.7	18.58	79.41	9.865	20.67	2.389	13.22	1.149
MG-5-13	63.76	487.2	122.8	715.7	223.8	52.57	127.8	13.66	57.27	7.033	14.04	1.585	8.35	0.716
MG-5-14	59.66	502.9	133.4	790.6	250.9	58.18	140.9	14.66	60.32	7.334	14.90	1.707	9.725	0.858
MG-5-15	90.41	691.7	174.7	1009.9	315.2	74.28	180.9	19.63	82.84	10.171	21.08	2.400	13.2	1.147
MG-5-16	66.65	514.6	129.7	754.0	234.7	54.88	134.0	14.17	58.94	7.210	14.70	1.656	9.02	0.7811
MG-5-17	69.77	532.1	133.5	770.0	237.2	55.29	135.0	14.13	58.25	7.104	14.56	1.658	9.19	0.824
MG-5-18	67.59	524.5	131.8	768.8	238.9	55.65	135.6	14.30	59.27	7.290	14.80	1.687	9.28	0.819
MG-5-19	99.32	715.4	171.3	957.5	282.4	65.35	155.4	16.18	66.19	7.979	16.02	1.782	9.56	0.817
MG-5-20	67.54	523.6	132.1	771.0	240.0	55.87	137.2	14.40	59.43	7.316	14.87	1.689	9.266	0.816

Table 3. Rare earth element content (ppm) of MG-6.

	La	Ce	Pr	Nd	Sm	Eu	Gd	Tb	Dy	Ho	Er	Tm	Yb	Lu
MG-6-1	64.07	522.5	134.4	785.6	247.7	56.53	138.2	13.95	55.57	6.881	14.22	1.753	11.38	1.210
MG-6-2	58.69	484.0	125.8	748.5	241.3	55.56	137.0	14.05	57.23	7.093	14.85	1.845	11.79	1.217
MG-6-3	64.10	543.8	144.7	885.8	300.4	71.00	180.8	19.23	79.70	9.980	21.35	2.666	17.2	1.819
MG-6-4	59.31	486.6	126.0	743.1	239.8	55.22	136.0	13.90	56.39	7.065	14.76	1.817	11.69	1.223
MG-6-5	102.70	761.7	182.3	997.2	283.4	61.75	144.4	13.94	53.83	6.420	12.96	1.563	9.71	0.982
MG-6-6	99.27	729.9	174.0	958.5	273.7	59.93	140.7	13.69	53.40	6.378	12.87	1.534	9.43	0.922
MG-6-7	65.05	531.1	135.3	798.2	251.6	57.47	140.8	14.33	57.05	7.066	14.63	1.782	11.38	1.182
MG-6-8	64.43	541.9	143.1	873.7	297.0	69.64	177.0	18.73	77.45	9.675	20.75	2.557	16.61	1.749
MG-6-9	101.66	763.8	185.2	1039.0	307.5	69.15	164.6	16.72	67.20	8.235	16.96	2.022	12.18	1.167
MG-6-10	61.39	498.6	128.6	759.1	241.2	55.76	137.2	14.13	57.80	7.274	15.01	1.811	11.07	1.112
MG-6-11	101.31	761.5	185.2	1034.5	307.7	69.18	164.6	16.84	67.66	8.280	17.04	2.031	12.13	1.184
MG-6-12	59.55	484.7	124.2	731.5	230.2	52.96	127.7	13.11	53.24	6.633	13.68	1.654	10.06	0.988
MG-6-13	60.03	491.6	125.8	738.4	233.8	53.56	129.6	13.14	52.68	6.516	13.44	1.65	10.52	1.080
MG-6-14	65.50	550.3	145.4	890.2	303.7	71.89	183.2	19.55	80.81	10.215	21.87	2.715	17.39	1.836
MG-6-15	100.36	769.8	188.8	1067.0	321.5	72.25	171.4	17.3	68.59	8.308	17.17	2.124	13.81	1.43
MG-6-16	101.48	778.1	191.1	1079.0	326.0	73.59	175.4	17.87	71.09	8.629	17.82	2.208	14.06	1.454
MG-6-17	63.18	526.9	138.6	841.2	280.5	65.76	166.2	17.47	72.07	9.016	18.81	2.345	15.03	1.573
MG-6-18	59.89	486.4	125.1	737.0	232.8	53.51	129.4	13.23	53.71	6.652	13.79	1.660	10.15	0.999
MG-6-19	59.54	492.9	127.2	754.7	239.4	55.06	133.6	13.65	54.92	6.779	14.20	1.765	11.38	1.191
MG-6-20	98.19	722.4	173.6	971.2	280.6	62.69	147.8	14.66	58.18	6.994	14.16	1.662	9.85	0.935

Table 4. U–Pb dating data of MG-5.

Point	Isotopic Ratios								^{207}Pb Corrected Age	
	^{238}U/^{206}Pb	1σ	^{207}Pb/^{206}Pb	1σ	^{207}Pb/^{235}U	1σ	^{206}Pb/^{238}U	1σ	^{206}Pb/^{238}U	±σ
Mg-5-01	4.210526	1.431579	0.833	0.014	27.18	0.38	0.2375	0.0034	28.59291	32.64977
Mg-5-02	4.08998	1.390593	0.822	0.014	27.67	0.46	0.2445	0.0034	50.96108	33.38145
Mg-5-03	8.503401	1.360544	0.810	0.014	13.04	0.15	0.1176	0.0016	35.85306	16.00427
Mg-5-04	5.534034	1.383509	0.817	0.012	20.28	0.25	0.1807	0.0025	44.92061	22.32279
Mg-5-05	5.274262	2.162447	0.804	0.015	20.82	0.41	0.1896	0.0041	66.82096	26.94427
Mg-5-06	4.231909	1.735083	0.821	0.016	26.67	0.37	0.2363	0.0041	51.14577	35.41699
Mg-5-07	3.996803	1.518785	0.829	0.015	28.36	0.48	0.2502	0.0038	38.13497	35.96065
Mg-5-08	4.106776	1.314168	0.821	0.013	27.53	0.34	0.2435	0.0032	52.69982	31.64773
Mg-5-09	4.152824	1.495017	0.824	0.013	27.25	0.40	0.2408	0.0036	46.3405	31.3618
Mg-5-10	3.805175	1.52207	0.821	0.013	29.62	0.40	0.2628	0.004	56.86429	34.14393
Mg-5-11	5.422993	1.247289	0.820	0.014	20.76	0.26	0.1844	0.0023	41.41196	25.17982
Mg-5-12	8.591065	1.37457	0.804	0.014	12.85	0.15	0.1164	0.0016	41.07903	15.79509
Mg-5-13	3.558719	1.494662	0.825	0.015	31.84	0.47	0.281	0.0042	51.80851	40.26918
Mg-5-14	3.640335	1.710957	0.835	0.014	31.54	0.51	0.2747	0.0047	28.66183	37.79578
Mg-5-15	8.833922	1.501767	0.798	0.014	12.44	0.16	0.1132	0.0017	45.387	15.32068
Mg-5-16	4.260758	1.533873	0.814	0.013	26.29	0.37	0.2347	0.0036	63.92638	30.37737
Mg-5-17	4.450378	1.691144	0.826	0.014	25.57	0.34	0.2247	0.0038	39.65274	30.76729
Mg-5-18	4.317789	1.554404	0.836	0.015	26.62	0.41	0.2316	0.0036	22.31356	33.43115
Mg-5-19	5.104645	1.327208	0.824	0.014	22.27	0.30	0.1959	0.0026	37.71706	26.80495
Mg-5-20	4.249894	1.529962	0.827	0.015	26.89	0.36	0.2353	0.0036	39.63593	33.78872

Table 5. U–Pb dating data of MG-6.

Point	Isotopic Ratios								^{207}Pb Corrected Age	
	^{238}U/^{206}Pb	1σ	^{207}Pb/^{206}Pb	1σ	^{207}Pb/^{235}U	1σ	^{206}Pb/^{238}U	1σ	^{206}Pb/^{238}U	±σ
Mg-6-01	4.892368	1.320939	0.817	0.013	23.10	0.32	0.2044	0.0027	42.88900	25.15391
Mg-6-02	5.698006	1.538462	0.822	0.014	19.86	0.24	0.1755	0.0027	29.76397	22.87941
Mg-6-03	7.446016	1.340283	0.818	0.014	15.14	0.18	0.1343	0.0018	27.11887	17.49094
Mg-6-04	4.940711	1.333992	0.812	0.012	22.71	0.29	0.2024	0.0027	50.61581	23.47389
Mg-6-05	4.901961	1.470588	0.826	0.011	23.17	0.25	0.204	0.003	28.01006	22.50032
Mg-6-06	2.84576	2.475811	0.823	0.008	39.90	1.00	0.3514	0.0087	57.80704	32.76922
Mg-6-07	4.863813	1.215953	0.824	0.013	23.33	0.33	0.2056	0.0025	31.54496	25.39222
Mg-6-08	7.36377	1.251841	0.825	0.014	15.46	0.23	0.1358	0.0017	19.75142	17.73803
Mg-6-09	8.591065	1.030928	0.802	0.009	12.91	0.14	0.1164	0.0012	38.43003	11.50474
Mg-6-10	4.391744	1.449275	0.828	0.013	25.92	0.32	0.2277	0.0033	27.58666	28.17365
Mg-6-11	8.826125	1.147396	0.805	0.011	12.62	0.13	0.1133	0.0013	34.76102	12.3742
Mg-6-12	4.413063	1.500441	0.827	0.014	25.83	0.34	0.2266	0.0034	29.28097	29.58775
Mg-6-13	4.863813	1.799611	0.832	0.014	23.59	0.38	0.2056	0.0037	18.27579	26.91974
Mg-6-14	7.651109	1.453711	0.811	0.014	14.60	0.18	0.1307	0.0019	33.76972	16.97535
Mg-6-15	7.102273	1.5625	0.809	0.012	15.73	0.30	0.1408	0.0022	38.64302	16.33509
Mg-6-16	7.942812	1.191422	0.809	0.009	14.05	0.13	0.1259	0.0015	34.35823	12.57437
Mg-6-17	6.72495	1.34499	0.821	0.012	16.83	0.21	0.1487	0.002	26.42441	17.34914
Mg-6-18	3.526093	2.679831	0.824	0.011	32.14	0.88	0.2836	0.0076	43.48483	31.21685
Mg-6-19	5.13347	1.488706	0.819	0.014	21.89	0.29	0.1948	0.0029	37.74075	25.35068
Mg-6-20	5.405405	1.135135	0.816	0.013	20.76	0.23	0.1850	0.0021	40.31684	22.76337

References

1. Cao, M.; Qin, K.; Li, G.; Evans, N.J.; Jin, L. In situ LA-(MC)-ICP-MS trace element and Nd isotopic compositions and genesis of polygenetic titanite from the Baogutu reduced porphyry Cu deposit, Western Junggar, NW China. *Ore Geol. Rev.* **2015**, *65*, 940–954. [CrossRef]
2. Harlov, D.; Tropper, P.; Seifert, W.; Nijland, T.; Förster, H.-J. Formation of Al-rich titanite ($CaTiSiO_4O$–$CaAlSiO_4OH$) reaction rims on ilmenite in metamorphic rocks as a function of fH_2O and fO_2. *Lithos* **2006**, *88*, 72–84. [CrossRef]
3. Li, J.-W.; Deng, X.-D.; Zhou, M.-F.; Liu, Y.-S.; Zhao, X.-F.; Guo, J.-L. Laser ablation ICP-MS titanite U–Th–Pb dating of hydrothermal ore deposits: A case study of the Tonglushan Cu–Fe–Au skarn deposit, SE Hubei Province, China. *Chem. Geol.* **2010**, *270*, 56–67. [CrossRef]
4. Kretz, R. Symbols for rock-forming minerals. *Am. Mineral.* **1983**, *68*, 277–279.
5. Kohn, M.J. Titanite Petrochronology. *Rev. Mineral. Geochem.* **2017**, *83*, 419–441. [CrossRef]
6. Higgins, J.B.; Ribbe, P.H. The crystal chemistry and space groups of natural and synthetic titanites. *Am. Mineral.* **1976**, *61*, 878–888.
7. Xu, B.; Hou, Z.-Q.; Griffin, W.L.; O'Reilly, S.Y.; Zheng, Y.-C.; Wang, T.; Fu, B.; Xu, J.-F. In-situ mineralogical interpretation of the mantle geophysical signature of the Gangdese Cu-porphyry mineral system. *Gondwana Res.* **2022**, *111*, 53–63. [CrossRef]

8. Fineberg, S.J.; Nandyala, S.V.; Marquez-Lara, A.; Oglesby, M.; Patel, A.A.; Singh, K. Incidence and risk factors for postoperative delirium after lumbar spine surgery (Phila Pa 1976). *Spine* **2013**, *38*, 1790–1796. [CrossRef]
9. Yu, J.-X.; Xu, B.; Zhao, Y.; Wang, Z.-X.; Zhang, Y.-F.; Kou, G.-Y. In situ Sr-O isotopic and elemental compositions of apatite and zircon from Pengcuolin granodiorites: Implications for Jurassic metallogenic variation in the southern tibet. *Ore Geol. Rev.* **2022**, *145*, 104869. [CrossRef]
10. Bonamici, C.E.; Fanning, C.M.; Kozdon, R.; Fournelle, J.H.; Valley, J.W. Combined oxygen-isotope and U–Pb zoning studies of titanite: New criteria for age preservation. *Chem. Geol.* **2015**, *398*, 70–84. [CrossRef]
11. Kohn, M.J.; Corrie, S.L. Preserved Zr-temperatures and U–Pb ages in high-grade metamorphic titanite: Evidence for a static hot channel in the Himalayan orogen. *Earth Planet. Sci. Lett.* **2011**, *311*, 136–143. [CrossRef]
12. Smith, M.; Storey, C.; Jeffries, T.E.; Ryan, C.G. In Situ U–Pb and Trace Element Analysis of Accessory Minerals in the Kiruna District, Norrbotten, Sweden: New Constraints on the Timing and Origin of Mineralization. *J. Pet.* **2009**, *50*, 2063–2094. [CrossRef]
13. Aleinikoff, J.N.; Wintsch, R.P.; Fanning, C.M.; Dorais, M.J. U–Pb geochronology of zircon and polygenetic titanite from the Glastonbury Complex, Connecticut, USA: An integrated SEM, EMPA, TIMS, and SHRIMP study. *Chem. Geol.* **2002**, *188*, 125–147. [CrossRef]
14. Paul, A.N.; Spikings, R.A.; Ulianov, A.; Ovtcharova, M. High temperature (>350 °C) thermal histories of the long lived (>500 Ma) active margin of Ecuador and Colombia: Apatite, titanite and rutile U–Pb thermochronology. *Geochim. Cosmochim. Acta* **2018**, *228*, 275–300. [CrossRef]
15. Schoene, B.; Bowring, S.A. Determining accurate temperature–time paths from U–Pb thermochronology: An example from the Kaapvaal craton, southern Africa. *Geochim. Cosmochim. Acta* **2007**, *71*, 165–185. [CrossRef]
16. Archibald, D.B.; Macquarrie, L.M.; Murphy, J.B.; Strachan, R.A.; McFarlane, C.R.; Button, M.; Larson, K.P.; Dunlop, J. The construction of the Donegal composite batholith, Irish Caledonides: Temporal constraints from U–Pb dating of zircon and titanite. *GSA Bull.* **2021**, *33*, 2335–2354. [CrossRef]
17. Xiao, X.; Zhou, T.; White, N.C.; Zhang, L.; Fan, Y.; Chen, X. Multiple generations of titanites and their geochemical characteristics record the magmatic-hydrothermal processes and timing of the Dongguashan porphyry-skarn Cu-Au system, Tongling district, Eastern China. *Miner. Deposita* **2020**, *56*, 363–380. [CrossRef]
18. Li, J.; Xu, L.L.; Bi, X.W.; Tang, Y.Y.; Sheng, X.Y.; Yu, H.J.; Liu, G.; Ma, R. New titanite U–Pb and molybdenite Re–Os ages for a hydrothermal vein-type Cu deposit in the Lanping Basin, Yunnan, SW China: Constraints on regional metallogeny and implications for exploration. *Miner. Deposita* **2020**, *56*, 441–456. [CrossRef]
19. Hart-Madigan, L.; Wilkinson, J.J.; Lasalle, S.; Armstrong, R.N. U–Pb dating of hydrothermal titanite resolves multiple phases of propylitic alteration in the Oyu tolgoi porphyry district, mongolia. *Econ. Geol.* **2020**, *115*, 1605–1618. [CrossRef]
20. Cao, M.; Qin, K.; Evans, N.J.; Li, G.; Ling, X.; McInnes, B.I.A.; Zhao, J. Titanite in situ SIMS U–Pb geochronology, elemental and Nd isotopic signatures record mineralization and fluid characteristics at the Pusangguo skarn deposit, Tibet. *Miner. Deposita* **2020**, *56*, 907–916. [CrossRef]
21. Olierook, H.K.; Taylor, R.J.; Erickson, T.M.; Clark, C.; Reddy, S.M.; Kirkland, C.L.; Jahn, I.; Barham, M. Unravelling complex geologic histories using U–Pb and trace element systematics of titanite. *Chem. Geol.* **2018**, *504*, 105–122. [CrossRef]
22. Song, S.; Mao, J.; Xie, G.; Chen, L.; Santosh, M.; Chen, G.; Rao, J.; Ouyang, Y. In situ LA-ICP-MS U–Pb geochronology and trace element analysis of hydrothermal titanite from the giant Zhuxi W (Cu) skarn deposit, South China. *Miner. Deposita* **2018**, *54*, 569–590. [CrossRef]
23. Gawęda, A.; Szopa, K.; Chew, D.; O'Sullivan, G.J.; Burda, J.; Klötzli, U.; Golonka, J. Variscan post-collisional cooling and uplift of the Tatra Mountains crystalline block constrained by integrated zircon, apatite and titanite LA-(MC)-ICP-MS U–Pb dating and rare earth element analyses. *Chem. Geol.* **2018**, *484*, 191–209. [CrossRef]
24. Fu, Y.; Sun, X.; Hollings, P.; Li, D.; Yang, T. Geochronology and trace element geochemistry of titanite in the Machangqing Cu-Mo-dominated polymetallic deposit, Yunnan Province, southwest China. *J. Southeast Asian Earth Sci.* **2018**, *158*, 398–414. [CrossRef]
25. Fu, Y.; Sun, X.; Zhou, H.; Lin, H.; Yang, T. In-situ LA–ICP–MS U–Pb geochronology and trace elements analysis of polygenetic titanite from the giant Beiya gold–polymetallic deposit in Yunnan Province, Southwest China. *Ore Geol. Rev.* **2016**, *77*, 43–56. [CrossRef]
26. Xu, L.; Bi, X.; Hu, R.; Tang, Y.; Wang, X.; Xu, Y. LA-ICP-MS mineral chemistry of titanite and the geological implications for exploration of porphyry Cu deposits in the Jinshajiang—Red River alkaline igneous belt, SW China. *Miner. Pet.* **2014**, *109*, 181–200. [CrossRef]
27. Paul, A.N.; Spikings, R.A.; Chew, D.; Daly, J.S. The effect of intra-crystal uranium zonation on apatite U–Pb thermochronology: A combined ID-TIMS and LA-MC-ICP-MS study. *Geochim. Cosmochim. Acta* **2019**, *251*, 15–35. [CrossRef]
28. Cochrane, R.; Spikings, R.A.; Chew, D.; Wotzlaw, J.-F.; Chiaradia, M.; Tyrrell, S.; Schaltegger, U.; van der Lelij, R. High temperature (>350 °C) thermochronology and mechanisms of Pb loss in apatite. *Geochim. Cosmochim. Acta* **2014**, *127*, 39–56. [CrossRef]
29. Kennedy, A.K.; Kamo, S.L.; Nasdala, L.; Timms, N. Grenville skarn titanite: Potential reference material for Sims U-Th-Pb analysis. *Can. Miner.* **2010**, *48*, 1423–1443. [CrossRef]
30. RRUFF Database. Available online: https://rruff.info/titanite/display=default/ (accessed on 1 June 2022).
31. Phyo, M.M.; Bieler, E.; Franz, L.; Balmer, W.; Krzemnicki, M.S. Spinel from Mogok, Myanmar-A Detailed Inclusion Study by Raman Microspectroscopy and Scanning Electron Microscopy. *J. Gemmol.* **2019**, *36*, 418–435. [CrossRef]

32. Xu, B.; Hou, Z.-Q.; Griffin, W.L.; Lu, Y.; Belousova, E.; Xu, J.-F.; O'Reilly, S.Y. Recycled volatiles determine fertility of porphyry deposits in collisional settings. *Am. Miner.* **2021**, *106*, 656–661. [CrossRef]
33. Xu, B.; Griffin, W.L.; Xiong, Q.; Hou, Z.-Q.; O'Reilly, S.Y.; Guo, Z.; Pearson, N.J.; Gréau, Y.; Yang, Z.; Zheng, Y.-C. Ultrapotassic rocks and xenoliths from South Tibet: Contrasting styles of interaction between lithospheric mantle and asthenosphere during continental collision. *Geology* **2016**, *45*, 51–54. [CrossRef]
34. Seneewong-Na-Ayutthaya, M.; Chongraktrakul, W.; Sripoonjan, T. Gemological Characterization of Peridot from Pyaung-Gaung in Mogok, Myanmar. *Gems Gemol.* **2022**, *57*, 318–337. [CrossRef]
35. Mitchell, A.; Htay, M.T.; Htun, K.M.; Win, M.N.; Oo, T.; Hlaing, T. Rock relationships in the Mogok metamorphic belt, Tatkon to Mandalay, central Myanmar. *J. Southeast Asian Earth Sci.* **2007**, *29*, 891–910. [CrossRef]
36. Xu, B.; Hou, Z.-Q.; Griffin, W.L.; Zheng, Y.-C.; Wang, T.; Guo, Z.; Hou, J.; Santosh, M.; O'Reilly, S.Y. Cenozoic lithospheric architecture and metallogenesis in Southeastern Tibet. *Earth-Science Rev.* **2020**, *214*, 103472. [CrossRef]
37. Nikischer, T. Gems & Mines of Mogok Ted Themelis. *Miner. News* **2010**, *26*, 10.
38. Zhang, D.; Guo, S.; Chen, Y.; Li, Q.; Ling, X.; Liu, C.; Sein, K. ~25 Ma Ruby Mineralization in the Mogok Stone Tract, Myanmar: New Evidence from SIMS U–Pb Dating of Coexisting Titanite. *Minerals* **2021**, *11*, 536. [CrossRef]
39. Searle, M.P.; Garber, J.M.; Hacker, B.R.; Htun, K.; Gardiner, N.J.; Waters, D.J.; Robb, L.J. Timing of Syenite-Charnockite Magmatism and Ruby and Sapphire Metamorphism in the Mogok Valley Region, Myanmar. *Tectonics* **2020**, *39*, e2019TC005998. [CrossRef]
40. Lamont, T.; Searle, M.; Hacker, B.; Htun, K.; Htun, K.M.; Morley, C.; Waters, D.; White, R. Late Eocene-Oligocene granulite facies garnet-sillimanite migmatites from the Mogok Metamorphic belt, Myanmar, and implications for timing of slip along the Sagaing Fault. *Lithos* **2021**, *386–387*, 106027. [CrossRef]
41. Xu, B.; Hou, Z.Q.; Griffin, W.L.; O'Reilly, S.Y. Apatite halogens and Sr–O and zircon Hf–O isotopes: Recycled volatiles in Jurassic porphyry ore systems in southern Tibet. *Chem. Geol.* **2022**, *10*, 120924. [CrossRef]
42. Win, M.M.; Enami, M.; Kato, T.; Thu, Y.K. A mechanism for Nb incorporation in rutile and application of Zr-in-rutile thermometry: A case study from granulite facies paragneisses of the Mogok metamorphic belt, Myanmar. *Miner. Mag.* **2017**, *81*, 1503–1521. [CrossRef]
43. Horie, K.; Hidaka, H.; Gauthier-Lafaye, F. Elemental distribution in apatite, titanite and zircon during hydrothermal alteration: Durability of immobilization mineral phases for actinides. *Phys. Chem. Earth Parts A/B/C* **2008**, *33*, 962–968. [CrossRef]
44. McDonough, W.F.; Sun, S.S. The composition of the Earth. *Chem. Geol.* **1995**, *120*, 223–253. [CrossRef]
45. Bonamici, C.E.; Blum, T.B. Reconsidering initial Pb in titanite in the context of in situ dating. *Am. Miner.* **2020**, *105*, 1672–1685. [CrossRef]
46. Ling, X.-X.; Li, Q.-L.; Huyskens, M.H.; Liu, Y.; Yin, Q.-Z.; Tang, G.-Q.; Li, J.; Zhang, H.-F.; Skublov, S.G.; Melnik, A.E.; et al. Matrix effects and improved calibration procedures for SIMS titanite U Pb dating. *Chem. Geol.* **2022**, *593*, 120755. [CrossRef]
47. Erdmann, S.; Wang, R.; Huang, F.; Scaillet, B.; Zhao, K.; Liu, H.; Chen, Y.; Faure, M. Titanite: A potential solidus barometer for granitic magma systems. *Comptes Rendus Geosci.* **2019**, *351*, 551–561. [CrossRef]
48. Hayden, L.A.; Watson, E.B.; Wark, D.A. A thermobarometer for sphene (titanite). *Contrib. Mineral. Petrol.* **2007**, *155*, 529–540. [CrossRef]
49. Pan, L.-C.; Hu, R.-Z.; Bi, X.-W.; Li, C.; Wang, X.-S.; Zhu, J.-J. Titanite major and trace element compositions as petrogenetic and metallogenic indicators of Mo ore deposits: Examples from four granite plutons in the southern Yidun arc, SW China. *Am. Miner.* **2018**, *103*, 1417–1434. [CrossRef]
50. Xie, L.; Wang, R.-C.; Chen, J.; Zhu, J.-C. Mineralogical evidence for magmatic and hydrothermal processes in the Qitianling oxidized tin-bearing granite (Hunan, South China): EMP and (MC)-LA-ICPMS investigations of three types of titanite. *Chem. Geol.* **2010**, *276*, 53–68. [CrossRef]
51. Xu, B.; Hou, Z.-Q.; Zheng, Y.-C.; Wang, R.; He, M.-Y.; Zhou, L.-M.; Wang, Z.-X.; He, W.-Y.; Zhou, Y.; Yang, Y. In situ elemental and isotopic study of diorite intrusions: Implication for Jurassic arc magmatism and porphyry Cu-Au mineralisation in southern Tibet. *Ore Geol. Rev.* **2017**, *90*, 1063–1077. [CrossRef]
52. Xu, B.; Hou, Z.Q.; Griffin, W.L.; Zhou, Y.; Zhang, Y.F.; Lu, Y.J.; Belousova, E.A.; Xu, J.F.; O'Reilly, S.Y. Elevated Magmatic Chlorine and Sulfur Concentrations in the Eocene–Oligocene Machangqing Cu–Mo Porphyry System. *SEG Spec. Publ.* **2021**, *24*, 257–276.